ELSEVIER

Nuclear Instruments and Methods in Physics Research B 140 (1998) 449–462

NIM B
Beam Interactions with Materials & Atoms

The response of gamma backscatter density gauges to spatial inhomogeneity – An extension of the single scattering model

A.J. Ball [a,*], C.J. Solomon [b], J.C. Zarnecki [a]

[a] *Unit for Space Sciences and Astrophysics, Physics Laboratory, University of Kent, Canterbury, Kent, CT2 7NR, UK*
[b] *Applied Optics Group, School of Physical Sciences, University of Kent, Canterbury, Kent, CT2 7NR, UK*

Received 25 August 1997; received in revised form 19 January 1998

Abstract

The single scattering model for gamma backscatter density gauges has been extended to describe how the total detected count rate changes in response to localised density variations within the material. This extended model suggests there is a spatial region where density perturbations have a contradictory effect on the measured density value, an effect that has already been shown experimentally by previous workers. Here we compare their results with those predicted by application of the extended single scattering model. Since a complete description of their experimental apparatus was not available, only a crude fit could be achieved. Nevertheless, all the basic features of the data could be reproduced. © 1998 Elsevier Science B.V.

PACS: 06.30.Dr; 07.85.-m; 81.70.-q; 93.85.+q
Keywords: Density measurement; Backscatter; Spatial response; Inhomogeneity

1. Introduction

Gamma backscatter density gauges use the Compton scattering of γ ray photons in bulk material to measure density. A source of γ photons (usually 662 keV from a collimated ^{137}Cs source) is placed at the surface of the bulk sample to inject gamma photons into the material. A detector is placed a short distance along the surface from the source to count photons scattered out of the material. Shielding of the source prevents photons reaching the detector directly. This arrangement is shown schematically in Fig. 1. The technique is widely used in borehole logging [1,2], soil science and the manufacturing and construction industries. It has even been adapted for use on the surfaces of the Moon, Mars and Venus [3]. Unlike transmission densitometers, where the linear geometry of source, sample and detector can be a limitation, backscatter density gauges can be applied to semi-infinite bulk materials (e.g. in situ measurement of rock or soil), boreholes or struc-

* Corresponding author. Present address: International Space Science Institute, Hallerstrasse 6, CH-3012 Bern, Switzerland; tel.: +41 31 6313254, fax: +41 31 6314897, e-mail: andrew.ball@issi.unibe.ch.

PII S0168-583X(98)00188-8

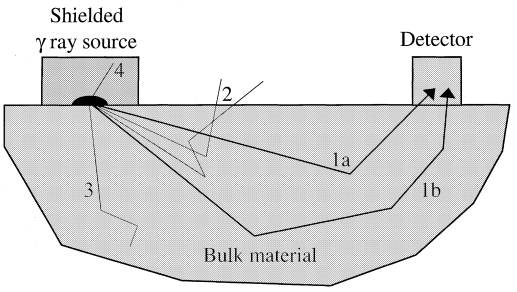

Fig. 1. Schematic diagram of a gamma backscatter density gauge. Photons emitted from the source are either: (1) detected having undergone single (a) or multiple (b) scattering in the material, (2) lost though the surface by single or multiple scattering in the material, (3) lost by scattering and absorption in the material, or (4) stopped by the source shielding.

tures where the other side is inaccessible (the walls of long tubes, for example).

Since the cross-section for Compton scattering is proportional to the number density of electrons, and the ratio of atomic mass to atomic number is 2.0, or nearly so, for all elements (except hydrogen), the backscattered count rate is a function of the bulk density. An approximate functional form for this calibration curve has been suggested [4]:

$$I(\rho) = K_1 \rho e^{-C_1 \rho} + K_2 \rho^2 e^{-C_2 \rho}, \quad (1)$$

where I is the total count rate detected, ρ is the material density and $K_{1,2}$ and $C_{1,2}$ are constants. This function is plotted in Fig. 2. The count rate reaches a maximum at some critical density, dependent on the sonde length (source-detector separation) and the source energy. Below this density the count rate falls due to the reduced concentration of electrons to scatter photons into the detector, while above this density the count rate falls due to the increased attenuation of the source beam. The two competing effects – scattering and attenuation – also form the focus of the extended model presented here, as discussed in Section 4.

At the ^{137}Cs source energy (662 keV), Compton scattering is the dominant interaction. At energies below about 150 keV the photoelectric effect is significant, while e^-/e^+ pair production occurs at energies above twice the electron rest mass energy (1.02 MeV). Both these processes have mass attenuation coefficients that are heavily dependent on

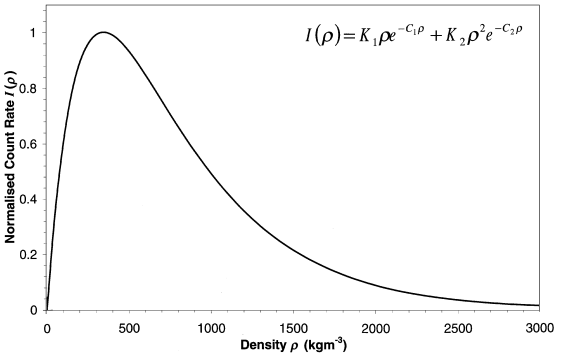

Fig. 2. Example calibration curve for a gamma backscatter densitometer, showing detected count rate vs. density, normalised to the maximum. The parameters are from Hearst and Carlson [4]: $C_1 = 3.45$ m^3 kg^{-1}, $C_2 = 2.6$ m^3 kg^{-1}, $K_1 = 0.4754$ s^{-1} kg^{-1} m^3, $K_2 = 1.8735 \times 10^{-4}$ s^{-1} kg^{-2} m^6. Backscatter densitometers usually operate on materials with a density above the critical value, i.e. where an increase in count rate implies a decrease in density.

elemental composition, which is why only those source energies within the "Compton window" are useful for densitometry. [1]

1.1. Previous work on depth and volume of investigation

Eq. (1) assumes that the value of density ρ is either constant throughout the material or varies only on scales much smaller than the instrument's size. Many real materials such as soil show porosity or other density variations on macroscopic scales, however. It is thus important to understand the behaviour of backscatter density gauges in terms of their spatial response and response to density inhomogeneity. Reducing this question to the single linear dimension of depth below the surface, Czubek [7] notes that the range of investigation of such devices can be defined in a number of different ways. Several studies have been performed to answer the question, employing the single scattering model (SSM) [8], Monte Carlo methods [9–12] and experiment [8,13,14].

[1] Lower source energies such as 59.5 keV from ^{241}Am are sometimes used in cases where the elemental composition is known [5,6].

Picton et al. [11] discuss a number of alternative measures of "depth of investigation". The function $S_1(h)$ was defined by them as the fraction of the detected count rate which remains after the material beyond a depth h has been removed. However $S_1(h)$ was found to suggest that the instrument measures density to a greater depth than is actually the case, since photons with maximum penetration depths beyond h have nevertheless "sampled" shallower layers along the way. Although Picton et al. [11] and Gulin [15] define the region beyond h to be a vacuum (more easily achieved in a Monte Carlo simulation than in the laboratory), several sources report experiments where another material is used [13,14]. The IAEA experiments [13] reported the fractional change in count rate as an increasing thickness of glass is placed between a surface density gauge and a concrete block. Sherman and Locke [14] investigated borehole density gauges using nested cylindrical annuli of dry sand. The annuli were sequentially saturated with water, starting with the inner one. They then expressed the variation of response with depth as the ratio of the change in measured density (for saturation to a depth h) to the change measured once all the annuli had been saturated. Based on these approaches we can thus define an alternative response function $S_{1a}(h)$ as the ratio of the change in count rate (when the material from the surface to a depth h is changed) to the total change as $h \rightarrow \infty$. The functions $S_{1a}(h)$ (sometimes called "J-factor") and $S_1(h)$ give rise to the commonly used 50% and 90% response depths h_{50} and h_{90}. Taking the limit of an infinitesimal density change, Picton et al. [11] go further to define an improved function $S_2(h)$ as follows:

$$S_2(h) = \lim_{\Delta\rho \rightarrow 0} \left[\frac{\rho_a(\Delta\rho, h) - \rho_b}{\Delta\rho} \right], \qquad (2)$$

where the density of the material from the surface to a depth h has been increased with respect to that beyond from ρ_b to $\rho_b + \Delta\rho$, leading to an apparent density ρ_a, as measured by the instrument. Since the calibration curve can be considered linear over a sufficiently small density range, density can be replaced by count rate in the expression above. The function $S_2(h)$ is of course only one-dimensional so it does not carry any information regarding the variation of response in the two perpendicular directions.

Two types of importance function (which can potentially be evaluated in three dimensions) are also discussed by Picton et al. [11] as tools for measuring depth of investigation. One type is the flux of eventually detected photons, while the other is the spatial density of scattering events, ignoring photons which pass through unscattered. The latter can be approximated by the SSM [8] or determined accurately by Monte Carlo simulation [9]. A variation on this was used by Ao and Gardner [16], who chose to base the importance of a volume element on the proportion of photons emitted isotropically from that element which are eventually detected. It is not clear in their paper how the assumption of isotropic emission might affect the subsequent Monte Carlo analysis – neither the flux of incoming photons nor the differential scattering cross-section is actually isotropic. James [12] computed the "weights" of volume elements in material under a real device, using a correlated Monte Carlo perturbation technique. This work showed (positive) peaks in "weight" under both source and detector, decaying with both depth and lateral distance from the baseline.

While the function $S_2(h)$ represents the best measure so far proposed for depth of investigation, a three-dimensional equivalent would be useful. This would examine the effect on the measured density of increasing the density of a small volume element and would also be useful for studying the effect of inhomogeneities. While this can be achieved for specific cases by Monte Carlo simulation, we propose here an extension to the SSM to handle such a situation. The experimental results of Devlin and Taylor [8] reproduced in Fig. 3 show that a localised density perturbation can either increase or decrease the count rate depending on where in the material it is placed. This interesting effect seems not to be highlighted by any of the previous investigations discussed above. The physical reason for the effect is clear – the density reduction increases the count rate where the attenuating role of the material it replaces is dominant, while it reduces the count rate where scattering into the detector is the important effect. This is evident in Fig. 3, where the

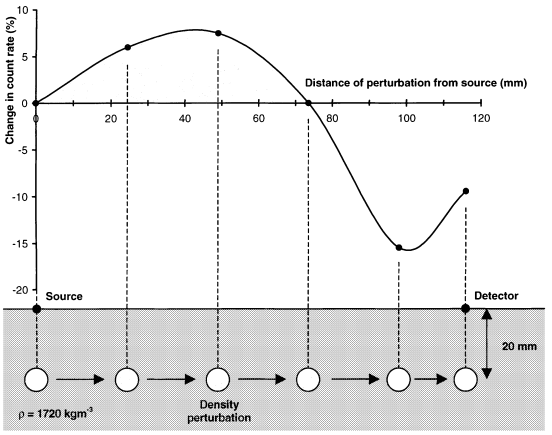

Fig. 3. Experimental results from Devlin and Taylor [8], showing that a localised decrease in density can either increase or decrease the detected count rate, depending where the perturbation is placed in the material.

count rate is increased in a region near the source but decreased in a region near the detector. The peaks (at about 40 and 100 mm, respectively) show where each of these effects is most important. Thus the apparent density measured by the instrument gives a false indication when the perturbation lies beyond about 74 mm from the source, assuming the instrument was operating in the regime where a decrease in bulk density should give an increase in count rate.

Devlin and Taylor used the SSM to generate maps of the density of scattering events in a hemispherical volume under the instrument – a quantity that is of course positive everywhere. We shall show that it is possible to extend the model to show the two regions implied by the results in Fig. 3.

In Section 2 we define the single scattering model, as introduced by Uemura [17] and Taylor and Kansara [18]. Section 3 revisits the spatial distribution of scattering events as outlined by Devlin and Taylor [8], including the evaluation of scatter density vs. depth. This is then extended in Section 4 to examine the effect on the total count rate (and hence measured density) of a small localised density change. Section 5 compares results from the extended SSM with the experimental results published by Devlin and Taylor.

2. Basic definition of the single scattering model (SSM)

The SSM has been used for many years [17,18,8] to explain the basic behaviour of backscatter densitometers. Monte Carlo methods are preferred for modelling real devices [10,12,19] but the SSM can nevertheless be of use to examine basic features of the measurement technique.

The SSM assumes that photons reaching the detector have been scattered only once in the material. This assumption is not valid for real instruments which have large source-detector separations or operate on particularly high densities (the upper limit scale length for single scattering being the attenuation length of source photons in the material). Despite this, however, the competition between scattering and absorption must still exist outside the domain of the SSM. Hence we may expect the SSM to retain some qualitative importance even in the multiple scattering regime. The basic geometry for a surface density gauge is shown in Fig. 4, though the model can easily be adapted for the cylindrical geometry of borehole devices. Photons of energy E emitted from a source at S propagate into the semi-infinite material underneath the device. A detector of sensitive area A is placed on the surface at a distance d (the sonde length) from the source. Both the source and detector are considered to be point-like in order to simplify the geometry and subsequent analysis.

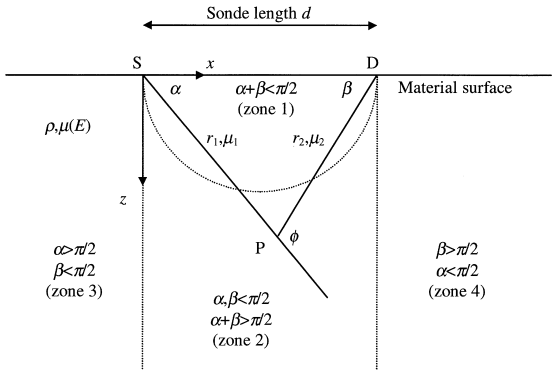

Fig. 4. Basic geometry of the single scattering model, showing the photon path SPD through the material from the source S to the detector D.

A general path for singly scattered photons is shown in Fig. 4, the emission direction being at an angle α to the baseline SD. Compton scattering is assumed to occur at a point P in the material, though some proportion of the photons may not reach P, having undergone absorption or scattering somewhere along the path SP of length r_1. Those photons scattered at P towards the detector make an angle β with the baseline, and may of course be lost along the path PD (of length r_2). The plane of the photon path SPD may be at some angle θ $\left(-\frac{1}{2}\pi < \theta < +\frac{1}{2}\pi\right)$ to the downward vertical. The point P may be defined either in Cartesian co-ordinates (x,y,z) or by the angular co-ordinates (α,β,θ) together with the sonde length d.

The material under investigation is assumed to be of uniform density ρ. The mass attenuation coefficient μ for photons is a function of their energy. Since we assume a mono-energetic source (such as the most commonly used radioisotope ^{137}Cs, which emits at 662 keV), the attenuation coefficient μ_1 for primary photons is fixed (at about 7.7×10^{-3} m^2 kg^{-1}). However, the mass attenuation coefficient for scattered photons (μ_2) varies with the scattering angle (ϕ), since the scattered photon energy E' is related to ϕ by the Compton formula (3). Note that E and E' are dimensionless since they are the ratio of photon energy over the electron mass-energy $m_e c^2$ ($=511$ keV).

$$E' = \frac{E}{1 + E(1 - \cos\ \phi)}. \tag{3}$$

For computing μ_2 we used an energy dependence approximated by a cubic function fitted to tabulated Compton cross-section data (from [20]) for the appropriate composition (SiO_2 was used for all the examples in this paper since quartz sand is a common test material). The fit was done in log–log space so the function $\mu(E)$ was of the following form:

$$\log_{10}\ \mu(E) = a_1 + a_2\ \log_{10}\ E + a_3(\log_{10}\ E)^2 + a_4(\log_{10}\ E)^3, \tag{4}$$

where $a_{1,2,3,4}$ are fitted coefficients ($a_1 = -2.0715$, $a_2 = -0.38455$, $a_3 = -0.020659$, $a_4 = 0.089562$).

Using simple trigonometry we can obtain the basic relations (5)–(8) between the angular and linear parameters in the diagram. These are useful when transforming between angular and Cartesian co-ordinate systems and when writing computer codes for the SSM.

$$r_1^2 = x^2 + y^2 + z^2, \qquad r_2^2 = (x - d)^2 + y^2 + z^2, \tag{5}$$

$$r_1 = \frac{d\ \sin\ \beta}{\sin\ \phi}, \qquad r_2 = \frac{d\ \sin\ \alpha}{\sin\ \phi}, \tag{6}$$

$$\phi = \alpha + \beta, \tag{7}$$

$$\alpha = \tan^{-1}\frac{\sqrt{y^2 + z^2}}{x}, \qquad \beta = \tan^{-1}\frac{\sqrt{y^2 + z^2}}{d - x}. \tag{8}$$

In Fig. 4 the dotted lines define four zones according to whether the angles α or β are greater than or less than $\frac{1}{2}\pi$. We shall see that, as one would expect, most of the scattering leading to detection occurs in zone 1. This is also significant in that scattering angles there are less than $\frac{1}{2}\pi$, which (due to Eq. (3)) limits the energy loss of ^{137}Cs photons to avoid lower energies where the interaction cross-section (and thus the density measurement) becomes much more composition dependent.

3. Distribution of scattering events for detected photons

To examine the count rate detected using the SSM we first need to consider a small volume element $\mathrm{d}V$ at P, scattering photons towards the detector. The geometry of the volume element $\mathrm{d}V$ in angular co-ordinates is shown in Fig. 5.

Consider a count rate $\mathrm{d}I$ resulting from scattering in the volume element $\mathrm{d}V$. The primary photon flux emitted from the source is subject to both the inverse square law and exponential attenuation by the material. The differential scattering cross-section is given by the Klein–Nishina formula [21]. The scattered flux is also subject to the inverse square law and exponential attenuation, though the mass attenuation coefficient is different for scattered photons, which are of lower energy than the primary photons. The detection of scattered photons depends on the area of the detector as well as the geometric factor resulting from the smaller projected area seen by photons incident at oblique angles. Hence that part $\mathrm{d}I$ of the detected count

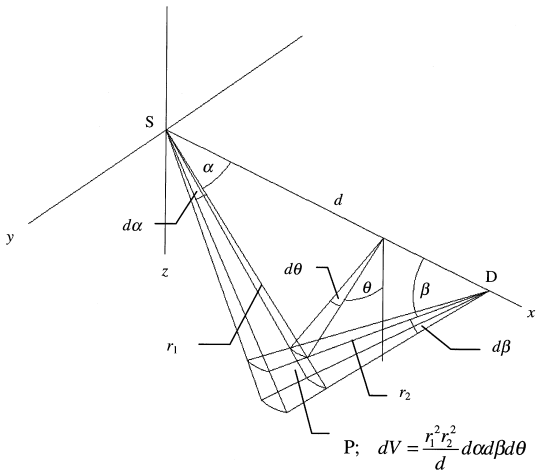

Fig. 5. Three-dimensional geometry of the volume element dV at the scattering point P defined by (α,β,θ) and d.

rate resulting from scattering at P is given initially by the following "word equation":

$$\begin{aligned}\mathrm{d}I = {} & \text{flux from source (photons m}^{-2}\text{ s}^{-1}\text{)} \\ & \times \text{ exponential attenuation factors along primary and scattered photon paths} \\ & \times \text{ number of electrons in volume element} \\ & \times \text{ differential cross-section (m}^2\text{)} \\ & \times \text{ solid angle subtended by the detector at the volume element.}\end{aligned}$$

Therefore,

$$\mathrm{d}I = \frac{S}{4\pi r_1^2}\exp[-\rho(\mu_1 r_1 + \mu_2 r_2)] \times n\mathrm{d}V\frac{\mathrm{d}\sigma}{\mathrm{d}\Omega}\frac{A\ \sin\ \beta\ \cos\ \theta}{r_2^2}, \tag{9}$$

where S is the source activity (photons s^{-1}) and n is the number density of electrons in the material.

The differential cross-section dσ/dΩ for Compton scattering of a photon of initial energy E is given by the Klein–Nishina formula (10).

$$\frac{\mathrm{d}\sigma}{\mathrm{d}\Omega} = \frac{r_0^2}{2}[1+E(1-\cos\ \phi)]^{-2}\left[1+\cos^2\ \phi + \frac{E^2(1-\cos\ \phi)^2}{1+E(1-\cos\ \phi)}\right], \tag{10}$$

where r_0 is the classical electron radius. Using Eq. (3) to generate the substitution

$$P(E,\phi) = [1+E(1-\cos\ \phi)]^{-1} \tag{11}$$

simplifies Eq. (10) to

$$\frac{\mathrm{d}\sigma}{\mathrm{d}\Omega} = \frac{r_0^2}{2}\left(P - P^2\ \sin^2\ \phi + P^3\right). \tag{12}$$

The electron number density n can be expressed in terms of mass density ρ, Avogadro's constant (N_A), the mean atomic number (Z) and the mean atomic mass (M) using the relation

$$n = \frac{N_A Z \rho}{M}. \tag{13}$$

Using Eq. (12) to substitute for dσ/dΩ in Eq. (9), and Eq. (13) to substitute for n gives us an expression (14) for dI including the functional dependence of the Klein–Nishina cross-section:

$$\mathrm{d}I = C\rho\left(P - P^2\ \sin^2\ \phi + P^3\right) \times \frac{\exp[-\rho(\mu_1 r_1 + \mu_2 r_2)]}{r_1^2 r_2^2}\sin\ \beta\ \cos\ \theta\ \mathrm{d}V, \tag{14}$$

where

$$C = \frac{SN_A Z A r_0^2}{8\pi M}. \tag{15}$$

Eq. (14) can be used to show graphically the density of scattering events (of detected photons) inside the material. Assuming a slice down through the material in the (x,z) plane (i.e. $\theta = 0$), the plot in Fig. 6 is obtained. The vertical axis is calibrated such that it shows the ratio of the detected scatter density to that which would be obtained if the detected scattering events were distributed uniformly through the hemispherical volume zone 1 ($= \pi d^3/12$). The scatter density at non-zero values of θ is simply less by a factor of cos θ. Two peaks in response are clearly visible, one under the detector and a smaller one under the source. The results obtained from this calculation are consistent with those shown by Devlin and Taylor [8], though they limited the calculation to zone 1. It should be noted that this distribution is for an uncollimated device – collimation can be included by setting limits for θ, α (for source collimation) and β (for detector collimation). A contour plot of the data in Fig. 6 is shown in Fig. 7.

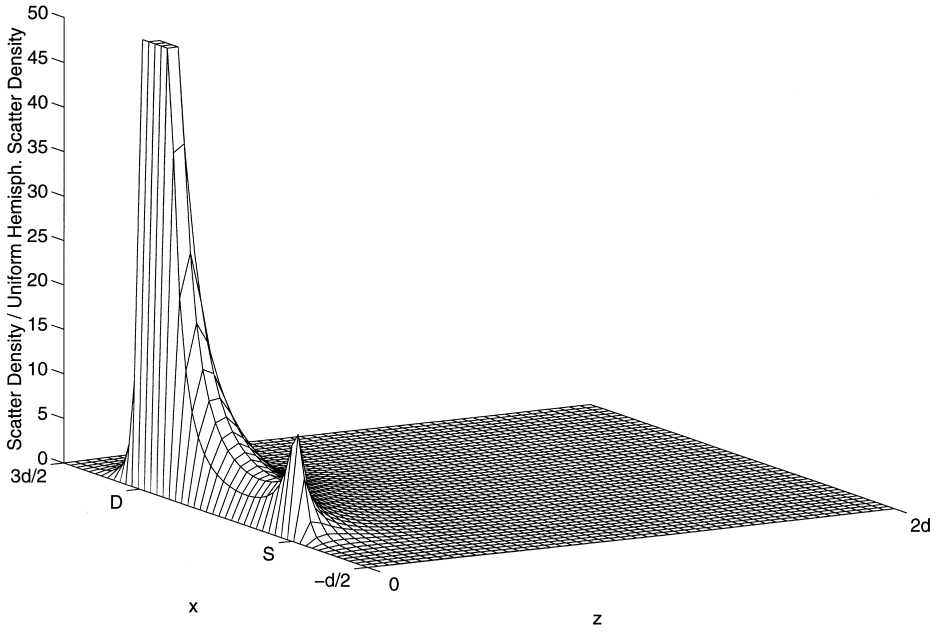

Fig. 6. Density of scattering events of detected photons, showing a slice down through the material in the (x,z) plane, for $-d/2 < x < 3d/2$ and $0 < z < 2d$. The quantity is normalised to the scatter density one obtains by assuming the scattering events to be distributed uniformly through the hemispherical volume zone 1. A large peak is visible below the detector D (truncated for clarity), while a smaller peak exists below the source S. Neither is actually a singularity due to the geometric factor $\sin\beta$ for the detector in Eq. (14). Input parameters for this plot are as follows: $E = 662$ keV, $d = 100$ mm and $\rho = 1000$ kg m^{-3}.

In Cartesian co-ordinates, however, it is difficult to see both the peaks and the low-level detail elsewhere. As an aid to visualisation it is useful to view the function on the (α,β) plane. As shown in Fig. 5, the volume element $\mathrm{d}V$ is given by

$$\mathrm{d}V = \frac{r_1^2 r_2^2}{d}\mathrm{d}\alpha\,\mathrm{d}\beta\,\mathrm{d}\theta. \tag{16}$$

Substituting Eq. (16) into Eq. (14) and expressing r_1 and r_2 in terms of α, β and d, we obtain an expression (17) for $\mathrm{d}I$ in the angular co-ordinate system (α,β,θ):

$$\mathrm{d}I = \frac{C\rho}{d}F_1(\alpha,\beta)\,\cos\,\theta\,\mathrm{d}\alpha\,\mathrm{d}\beta\,\mathrm{d}\theta, \tag{17}$$

where

$$F_1(\alpha,\beta) = \left(P - P^2\,\sin^2\,\phi + P^3\right) \times \exp\left[-\frac{\rho d(\mu_1\,\sin\,\beta + \mu_2\,\sin\,\alpha)}{\sin\,\phi}\right] \sin\,\beta. \tag{18}$$

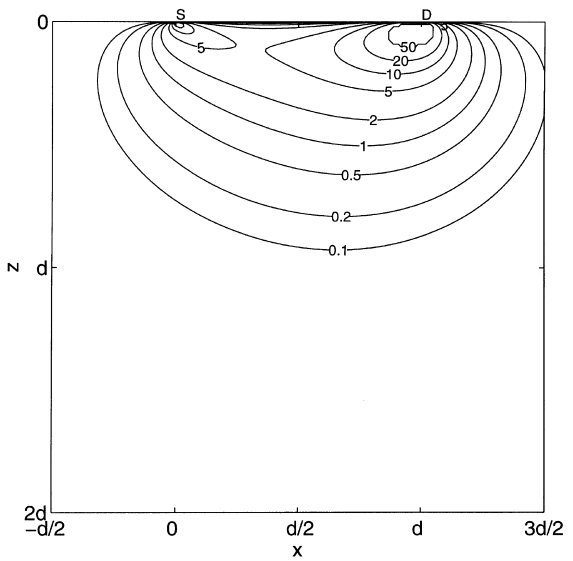

Fig. 7. Density of scattering events of detected photons, showing the same slice down through the material as in Fig. 6 and the same input parameters, but as a contour plot. Again the large peak below the detector is truncated for clarity.

The dimensionless function $F_1(\alpha,\beta)$ is shown in Fig. 8. This representation shows the angular dependence of the scattering and absorption more clearly by using a co-ordinate system more suited to the problem. Fig. 9 shows how the Cartesian co-ordinates x and z map onto the (α,β) plane. Contours of constant depth z are of the form

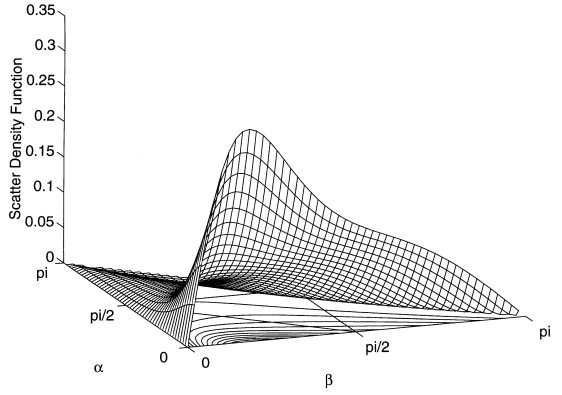

Fig. 8. Dimensionless scatter density function $F_1(\alpha,\beta)$. $F_1(\alpha,0)=0$ and $F_1(\alpha,\pi-\alpha)=0$. The fact that only a single peak is seen here compared to the Cartesian version in Fig. 6 is a result of the mapping to the (α,β) plane.

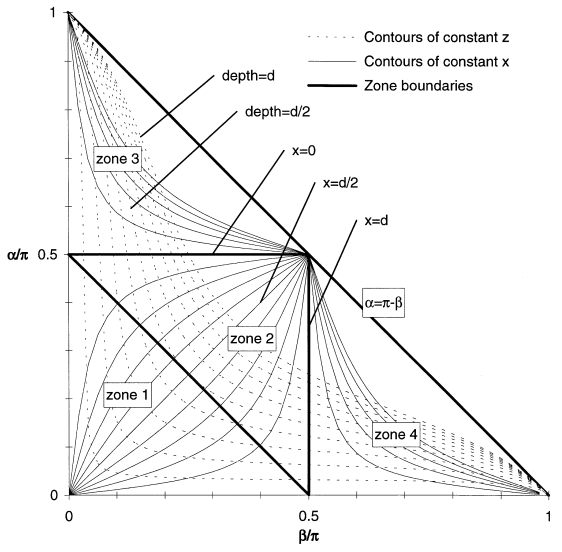

Fig. 9. Contours of constant z (depth) and x in (α,β) space ($\theta=0$). The four triangular zones correspond to those shown in Fig. 4. Values of z are from $d/10$ to d in steps of $d/10$. Values of x are from $-d/2$ to $+3d/2$ in steps of $d/10$.

$$\alpha = \cot^{-1}\left(\frac{d}{\sqrt{y^2+z^2}} - \cot\ \beta\right), \tag{19}$$

while those of constant x are of the form

$$\alpha = \tan^{-1}\left(\left(\frac{d}{x}-1\right)\tan\ \beta\right). \tag{20}$$

Integrating $F_1(\alpha,\beta)$ under contours of constant depth can be used to show how the density of scattering events varies with depth. The numerical integration (21) is easier to perform on the more well-behaved function $F_1(\alpha,\beta)$ than the Cartesian form:

$$\int_{z'=0}^{z} \mathrm{d}I = \frac{C\rho}{d}\int_{\theta=-\pi/2}^{+\pi/2}\int_{\beta=0}^{\pi}\int_{\alpha=0}^{\cot^{-1}\left((d\ \cos\ \theta)/z'-\cot\ \beta\right)} F_1(\alpha,\beta) \times \cos\ \theta\ \mathrm{d}\alpha\ \mathrm{d}\beta\ \mathrm{d}\theta. \tag{21}$$

The result of this integration (shown differentially and normalised to the integral for $z=\infty$) is shown in Fig. 10, for a density of 1000 kg m^{-3}. A FORTRAN code was used, including NAG numerical library routines D01AHF and D01DAF. As expected the density of scattering events leading to detection falls off almost exponentially with depth. The decay with normalised depth is steeper for greater sonde lengths since the unchanged attenu-

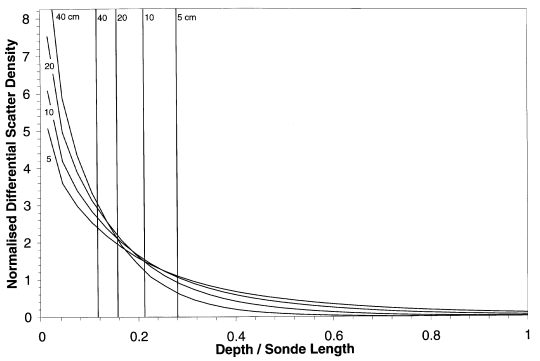

Fig. 10. Spatial density of scattering events leading to detection, plotted vs. depth into the material. The density of scattering events is normalised to the total (i.e. the area under each curve is unity). The depth is expressed as a fraction of the sonde length. The curves represent sonde lengths of 5, 10, 20 and 40 cm; in each case the mean depth is indicated. The results are for a material density of 1000 kg m^{-3}.

ation length becomes ever smaller in comparison. The mean depth data can be plotted as absolute depth vs. sonde length, as shown in Fig. 11. A power law fit shows that doubling the sonde length increases the mean depth by a factor of about 1.51. We leave it as an open question whether a similar figure can be determined for real devices.

4. Extension of the single scattering model

We shall now extend the SSM to examine the effect on the detected count rate (and hence measured density) of a small localised density change. Consider a small volume element dV at a general point P in the material, with enhanced density $\rho + \delta\rho_P$. The effect of this will be threefold, as illustrated in Fig. 12:

- The increased number of electrons will increase the scattering at P.
- The increased density will cause increased attenuation of primary photons.
- The increased density will cause increased attenuation of scattered photons.

We can adapt Eq. (17) to account for these three effects, producing an expression for the resultant change in count rate $\delta(dI)$ due to the density change in dV. Expressing $\delta(dI)$ as the sum of $\delta_1(dI)$, $\delta_2(dI)$ and $\delta_3(dI)$ for each of the three effects respectively, we obtain Eqs. (22), (24) and (25).

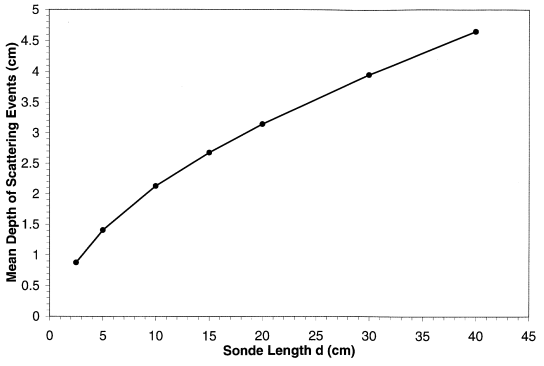

Fig. 11. Mean depth of scattering events leading to detection plotted vs. sonde length, as determined using the single scattering model. A power law fit gives an exponent of 0.5965 and a regression coefficient of 0.99925.

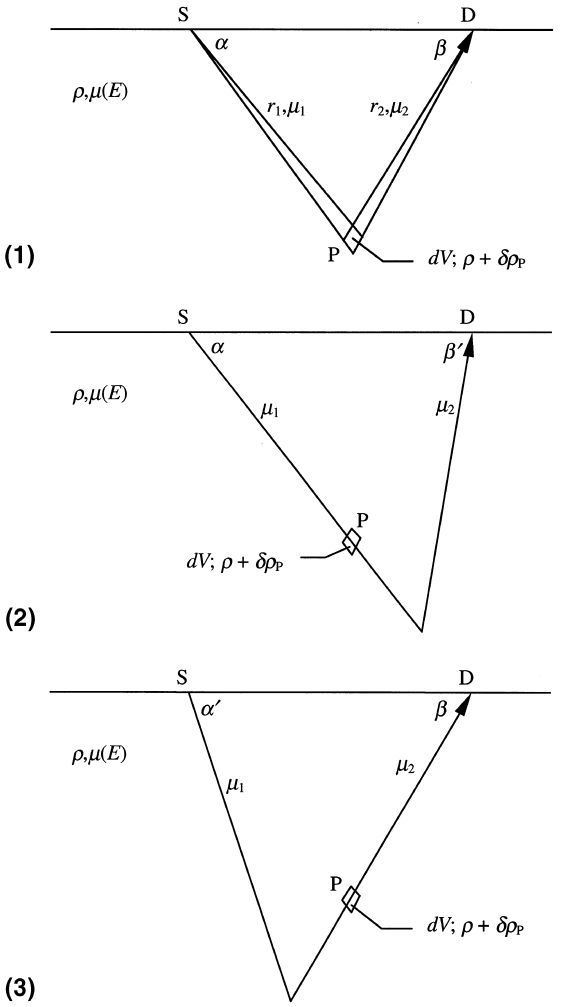

Fig. 12. Enhanced density in volume element dV at P has three effects: (1) increased number of scattering centres, (2) increased attenuation of primary photons, and (3) increased attenuation of scattered photons.

$$\delta_1(dI) = \frac{C}{d} F_2(\alpha,\beta)\ \sin\ \beta\ \cos\ \theta\, d\alpha\, d\beta\, d\theta\, \delta\rho_P, \quad (22)$$

where

$$F_2(\alpha,\beta) = \left(P - P^2\ \sin^2\ \phi + P^3\right) \times \exp\left[-\frac{\rho d(\mu_1\ \sin\ \beta + \mu_2\ \sin\ \alpha)}{\sin\ \phi}\right]. \quad (23)$$

Eq. (22) is equivalent to $dI \times \delta\rho_P/\rho$.

$$\delta_2(\mathrm{d}I) = -\frac{C\rho}{d}\left(\int_{\beta'=\beta}^{\pi-\alpha} F_2(\alpha,\beta')\ \sin\ \beta'\ \mathrm{d}\beta'\right) \times \cos\ \theta\ \mathrm{d}\alpha\ \mathrm{d}\theta(1-\exp[-\delta\rho_{\mathrm{P}}\mu_1 r_2 \mathrm{d}\beta]) \approx -\frac{C\rho}{\sin\ \phi}\mu_1\ \sin\ \alpha\left(\int_{\beta'=\beta}^{\pi-\alpha} F_2(\alpha,\beta')\sin\ \beta'\ \mathrm{d}\beta'\right) \times \cos\ \theta\ \mathrm{d}\alpha\ \mathrm{d}\beta\ \mathrm{d}\theta\ \delta\rho_{\mathrm{P}}. \quad (24)$$

$$\delta_3(\mathrm{d}I) = -\frac{C\rho}{d}\left(\int_{\alpha'=\alpha}^{\pi-\beta} F_2(\alpha',\beta)\ \mathrm{d}\alpha'\right) \times \sin\ \beta\ \cos\ \theta\ \mathrm{d}\beta\ \mathrm{d}\theta(1-\exp[-\delta\rho_{\mathrm{P}}\mu_2 r_1 \mathrm{d}\alpha]) \approx -\frac{C\rho}{\sin\ \phi}\mu_2\ \sin^2\ \beta\left(\int_{\alpha'=\alpha}^{\pi-\beta} F_2(\alpha',\beta)\ \mathrm{d}\alpha'\right) \times \cos\ \theta\ \mathrm{d}\alpha\ \mathrm{d}\beta\ \mathrm{d}\theta\ \delta\rho_{\mathrm{P}}. \quad (25)$$

Primary photon paths passing through the region of enhanced density always have angular co-ordinates β greater than that of point P, hence the integral expression for $\beta < \beta' \leqslant \pi - \alpha$ in Eq. (24). Similarly, for scattered photon paths passing through P there is an integral expression in Eq. (25) over the range $\alpha < \alpha' \leqslant \pi - \beta$. The primed co-ordinates are dummy variables. In Eqs. (24) and (25), the approximation made assumes the additional attenuation factor through the perturbed volume element to be small, i.e. $\delta\rho_{\mathrm{P}}\mu_1 r_2 \mathrm{d}\beta \ll 1$ and $\delta\rho_{\mathrm{P}}\mu_2 r_1 \mathrm{d}\alpha \ll 1$, respectively. This is reasonable since $\mathrm{d}\alpha$ and $\mathrm{d}\beta$ are infinitesimal.

By summing the three terms we obtain

$$\delta(\mathrm{d}I) = \frac{C}{d}\left[F_2(\alpha,\beta)\ \sin\ \beta - \frac{\rho d}{\sin\ \phi}\left(\mu_1\ \sin\ \alpha\int_{\beta'=\beta}^{\pi-\alpha} F_2\left(\alpha,\beta'\right)\ \sin\ \beta'\ \mathrm{d}\beta' + \mu_2\ \sin^2\ \beta\int_{\alpha'=\alpha}^{\pi-\beta} F_2(\alpha',\beta)\ \mathrm{d}\alpha'\right)\right] \cos\ \theta\ \mathrm{d}\alpha\ \mathrm{d}\beta\ \mathrm{d}\theta\ \delta\rho_{\mathrm{P}}. \quad (26)$$

This expression for sensitivity of total count rate to a small change in local density is not simply a differentiation of Eq. (17) with respect to density,

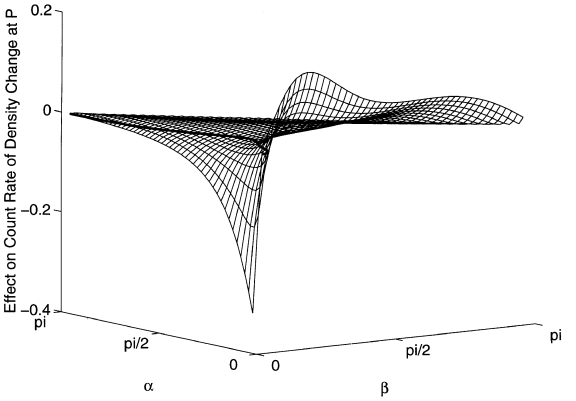

Fig. 13. Plot of the dimensionless function (27), showing the effect on count rate of small local changes $\delta\rho_{\mathrm{P}}$ in density, as a function of α and β. There are both positive and negative regions, showing that a local increase in density can either cause an increase or decrease in count rate, depending on the location of the density enhancement. The zero contour is shown to identify the boundary between positive and negative regions.

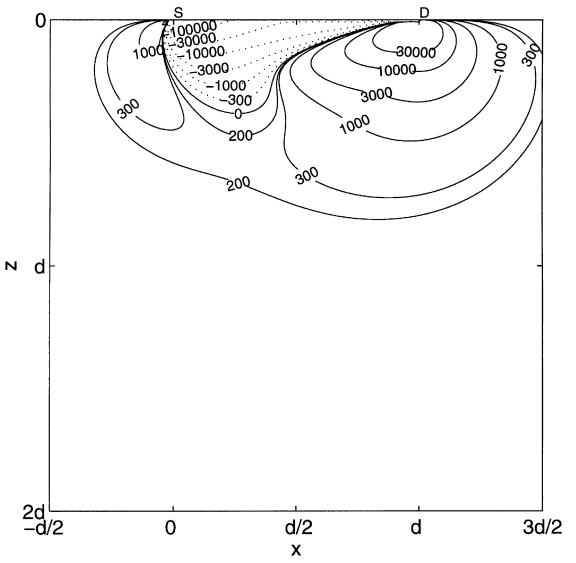

Fig. 14. Contour plot in Cartesian co-ordinates of (29), illustrating the sensitivity of the detected count rate to a localised density perturbation $\delta\rho_{\mathrm{P}}$. The contour values are in units of m^{-4}.

since we are now making a distinction between the local density ρ_P in the volume element dV and the bulk density ρ of the surrounding material.

Fig. 13 shows the dimensionless quantity

$$\frac{\delta(dI)d}{C\ \cos\ \theta\, d\alpha\, d\beta\, d\theta\, \delta\rho_P}, \tag{27}$$

i.e. the part which varies with α and β (again, the NAG library routine D01AHF was used). Clearly there are both positive and negative regions. This shows that a local increase in density can cause either an increase or decrease in count rate, depending on the location of the density enhancement. The location of the two regions can be seen plotted in Cartesian co-ordinates in Fig. 14, the units of which are m^{-4}.

To examine the function in Cartesian co-ordinates we can write

$$\delta(dI) = C\left[F_2(\alpha,\beta)\ \sin\ \beta - \frac{\rho d}{\sin\ \phi}\left(\mu_1\ \sin\ \alpha \int_{\beta'=\beta}^{\pi-\alpha} F_2\left(\alpha,\beta'\right)\ \sin\ \beta'\, d\beta' + \mu_2\ \sin^2\ \beta \int_{\alpha'=\alpha}^{\pi-\beta} F_2\left(\alpha',\beta\right) d\alpha'\right)\right]\frac{\cos\ \theta}{r_1^2 r_2^2} dV\ \delta\rho_P. \tag{28}$$

To show the functional part of this we plotted the quantity

$$\frac{\delta(dI)}{C\ \cos\ \theta\, dV\ \delta\rho_P} \tag{29}$$

(which has units of m^{-4}) in Fig. 14.

The existence of these two regions means that a localised change in density can actually cause the backscatter densitometer to give a false indication if the density variation is in the "wrong" region. Whether this is the case or not depends not only on whether Eq. (26) is positive or negative, but also whether $dI/d\rho$ is positive or negative on the calibration curve. Since most backscatter devices operate in the region where $dI(\rho)/d\rho < 0$, it is the positive region in Fig. 14 which will produce a contradictory response when a perturbation is introduced.

5. Comparison with experimental results

As a first test for the predictions of the extended SSM we tried to reproduce the results of Devlin and Taylor [8] shown in Fig. 3. The key parameters of their experiment were included in their paper ($d = 116$ mm, $\rho = 1720$ kg m^{-3}, depth of perturbation $= 20$ mm), with the exception of the size and density of the perturbing volume element. However, their diagram indicates a sphere perhaps 10 mm in diameter which they state was made of expanded polystyrene. This was assumed to have had a density of around 100 kg m^{-3}, much lower than that of the surrounding material. For the bulk material we assumed the mass attenuation coefficient of SiO_2 (as used in Sections 3 and 4) to be an adequate approximation for their "standard soil".

To derive a quantity equivalent to the percentage change in count rate quoted by Devlin and Taylor we evaluated Eq. (28) for the appropriate range of depths (centred on 20 mm) covered by the finite size of the perturbation, with $\theta = 0$. These were then combined, weighted according to the fractional volume of sphere present at each depth value. This quantity was then divided by the total count rate from Eq. (21) and multiplied by the value of $dV\ \delta\rho_P$ obtained using the radius of the sphere and the assumed density change (-1620 kg m^{-3}). In addition an offset was introduced to match the model to zero at the source, since the experimental data concerns the change relative to the count rate for the perturbation below the source, rather than uniform material.

The model was run for several sets of parameters, reflecting their uncertainty in the original experiment. The results are shown in Fig. 15 together with the experimental data. The model consistently shows the positive and negative peaks reported by Devlin and Taylor, however no single set of parameters produces a model that follows the data closely everywhere.

Assuming a radius of 5 mm, the model predicts a change in count rate far smaller than that reported. However, the degree of collimation of the source and detector may be responsible for reducing the total count rate and increasing the relative importance of the region where the perturbation is

placed. Collimation to limit the range of θ would have such an effect, for instance. Line A shows the model data amplified by a factor of 112 to match the peak heights of the data. The main difference in shape is that the model shows the negative peak to be nearer the detector. This could be the effect of detector collimation to limit β, concentrating the instrument on the region between source and detector. A good fit is obtained without an "artificial" amplification factor by increasing the radius of the perturbation to 19 mm (line B). Not only do both peaks match in height, the zero point between them also coincides with the data. The positive peak is now also displaced from the data, however.

The extended SSM clearly shows the two regions of opposite effect, though without better knowledge of the collimation and characteristics of the perturbing sphere in the original experiment it is difficult to match the model more closely. The location of the model's negative peak closer to the detector does suggest collimation in β, while the need for a large amplification factor to fit the model to the peak heights also suggests collimation in θ.

6. Conclusions and further work

This paper explains how the effect shown by Devlin and Taylor [8] can be examined by extending the single scattering model for gamma backscatter density gauges. Understanding how a backscatter density gauge responds to inhomogeneities in the target is clearly important since voids and density enhancements are common in natural materials.

Since the apparatus used by Devlin and Taylor is not fully described in their paper it is difficult to make a full comparison between the extended SSM and the data. However the basic features are reproduced by the model, namely a positive peak near the source and a negative peak near the detector. The positive peak is also seen to be broader than the negative one. Although the model cannot yet claim to reproduce quantitative results perfectly, it does provide a basic theoretical framework that could be extended further. Collimation and the energy dependence of the detector could certainly be incorporated, for instance. A Monte Carlo method would have to be applied to incorporate multiple scattering effects.

Since most real gauges operate in the regime where $dI(\rho)/d\rho < 0$, the most important "contradictory" region lies under the detector, where decreases in density *reduce* the count rate. This was shown in Fig. 14 for the example set of model parameters. Further investigation is required to show how the sizes and shapes of the regions change for different cases.

It is interesting to consider the effect on the count rate of a single perturbation as the density gauge passes over the surface parallel to the baseline, as is the case for borehole density logging. The count rate would rise and fall – or fall and rise – before returning to the response from the uniform material. The asymmetry between the positive and negative peaks (as seen in Fig. 15) could maybe be used to distinguish between positive and negative density perturbations. Simply applying the calibration curve to the count rate would incorrectly suggest adjacent regions of higher and lower density in the bulk material, rather than a single region of different density. Similar scenarios might be considered for stationary devices examining bubbles or solid lumps carried past the instrument in a liquid, or imperfections in a continuously produced material.

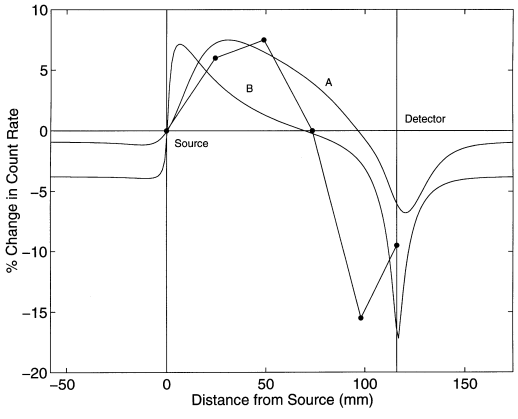

Fig. 15. Comparison of experimental data (connected points) from Devlin and Taylor [8] with results from the extended single scattering model (smooth lines).

The authors do not currently have access to facilities suitable for a comprehensive study of real backscatter density gauges, nor do they anticipate an in-depth application of Monte Carlo codes. Rather, it is hoped that other workers more directly involved in soil science, borehole logging or non-destructive testing might carry this topic forward. The current work evolved through evaluating methods by which the density of material at the surface of a cometary nucleus may be measured as part of the European Space Agency's *Rosetta* mission to comet 46P/Wirtanen [3,5,22]. The University of Kent together with University College London's Mullard Space Science Laboratory form part of the MUPUS experiment team selected to provide instruments on the *Rosetta Lander* for in situ measurement of the physical properties of the cometary surface material.

Acknowledgements

The authors acknowledge the financial assistance provided by the University of Kent's University Research Fund. A.J. Ball acknowledges the postgraduate studentship award provided by the Particle Physics and Astronomy Research Council (PPARC).

Appendix A. Summary of key mathematical symbols

Symbol(s)	Description
I	Total count rate detected at D, photons s^{-1}
dI	Number of photons per second from volume element dV scattered into the detector, photons s^{-1}
dV	Volume element at point P, m^3
S	Source activity, photons s^{-1}
n	Number density of electrons, m^{-3}
A	Area of detector (in (x,y) plane), m^2
$d\sigma/d\Omega$	Differential cross-section for Compton scattering, m^2
μ_1, μ_2	Mass attenuation coefficient of photon in the material before and after scattering, m^2 kg^{-1}
ρ	Bulk density of material, kg m^{-3}
ρ_P	Material density in volume element at P, kg m^{-3}
$\delta\rho_P$	Small change in ρ_P, kg m^{-3}
α, β	Angles of primary and scattered photon paths to the surface, rad
ϕ	The angle of scattering, equal to $\alpha + \beta$, rad
θ	Angle made by photon path to the downward vertical, rad
r_1, r_2	Length of primary and scattered photon paths, m
d	Source-detector separation (sonde length), m
r_0	Classical electron radius ($= e^2/(4\pi\varepsilon_0 m_e c^2) = 2.818 \times 10^{-15}$ m), m
E	Ratio of source photon energy relative to the electron mass-energy $m_e c^2$ ($= 511$ keV)

References

[1] J.J. Pickell, J.G. Heacock, Geophysics 25 (4) (1960) 891–904.
[2] J. Tittman, J.S. Wahl, The physical foundations of formation density logging (Gamma–Gamma), Geophysics 30 (1965) 284–294.
[3] A.J. Ball, Measuring Physical Properties at the Surface of a Comet Nucleus, Ph.D. Thesis, University of Kent, Canterbury, UK, submitted December 1997.
[4] J.R. Hearst, R.C. Carlson, Geophysics 34 (2) (1969) 222–234.
[5] A.J. Ball, C.J. Solomon, J.C. Zarnecki, Planet. Space Sci. 44 (3) (1996) 283–293.
[6] F. Divós, S. Szegedi, P. Raics, Holz als Roh- und Werkstoff 54 (4) (1996) 279–281.
[7] J.A. Czubek, Int. J. Appl. Radiat. Isot. 34 (1) (1983) 153–172.
[8] G. Devlin, D. Taylor, J. Soil Sci. 21 (2) (1970) 297–303.
[9] C.C. Watson, Numerical simulation of the litho-density tool lithology response, in: Proceedings of Soc. Petr. Engnrs. of AIME 58th Annual Tech. Conf., SPE-12051, 1983.
[10] J.S. Petler, IEEE Trans. Nucl. Sci. 37 (2) (1990) 954–958.
[11] D.J. Picton, R.G. Harris, K. Randle, D.R. Weaver, IEEE Trans. Nucl. Sci. 39 (4) (1992) 1014–1018.
[12] L.H. James, Nucl. Geophys. 7 (2) (1993) 343–352.

[13] IAEA, Commercial portable gauges for radiometric determination of the density and moisture content of building materials, IAEA Technical Reports Series 130, 1971.
[14] H. Sherman, S. Locke, Depth of investigation of neutron and density sondes for 35-percent-porosity sand, in: Trans. 16th Symp. Society of Professional Well Log Analysts 1975.
[15] Yu.A. Gulin, Gamma–Gamma Method of Investigation of Oil Wells, Nedra, Moscow, 1975, in Russian.
[16] Q. Ao, R.P. Gardner, Nucl. Geophys. 9 (6) (1995) 497–515.
[17] T. Uemura, Jpn. J. Appl. Phys. 4 (9) (1965) 667–676.
[18] D. Taylor, M. Kansara, Soil Sci. 104 (1) (1967) 25–34.
[19] D.J. Picton, R.G. Harris, K. Randle, D.R. Weaver, Nucl. Instr. and Meth. A 359 (3) (1995) 559–565.
[20] E. Storm, H.I. Israel, Nucl. Data Tables A 7 (1970) 565–681.
[21] O. Klein, Y. Nishina, Z. Phys. 52 (1929) 853–868.
[22] A.J. Ball, M.W. Trow, A. Smith, J.C. Zarnecki, Laboratory Development of the MUPUS Densitometer for the Rosetta Comet Lander, Poster PS076 at the European Geophysical Society, Vienna, 21–25 April 1997; Abstract in Annal. Geophys. 15 (suppl. III) (1997) C810.